01 Feb 2021

A High-Temperature-Resistant Inorganic Matrix for Concrete Structures Enhanced by Fiber-Reinforced Polymer

Jing Zhu

Wenzhong Zheng

Lili Xie

Lesley Sneed
Missouri University of Science and Technology, sneedlh@mst.edu

Recommended Citation

J. Zhu et al., "A High-Temperature-Resistant Inorganic Matrix for Concrete Structures Enhanced by Fiber-Reinforced Polymer," *Alexandria Engineering Journal*, vol. 60, no. 1, pp. 131-143, Elsevier, Feb 2021. The definitive version is available at https://doi.org/10.1016/j.aej.2020.06.021

HOSTED BY

ELSEVIER

Alexandria University

Alexandria Engineering Journal

www.elsevier.com/locate/aej
www.sciencedirect.com

AEJ JOURNAL

A high-temperature-resistant inorganic matrix for concrete structures enhanced by fiber-reinforced polymer

Check for updates

Jing Zhu [a],*, Wenzhong Zheng [b], Lili Xie [c], Lesley H. Sneed [d]

[a] *College of Civil Engineering and Architecture, Harbin University of Science and Technology, Harbin 150080, China*
[b] *Key Lab of Structures Dynamic Behavior and Control of the Ministry Education, Harbin Institute of Technology, Harbin 150090, China*
[c] *Key Laboratory of Earthquake Engineering and Engineering Vibration, Institute of Engineering Mechanics, China Earthquake Administration, Harbin 150080, China*
[d] *Department of Civil, Architectural and Environmental Engineering, Missouri University of Science and Technology, Rolla, MO 65401, USA*

Abstract This paper probed deep into a high-temperature resistant inorganic matrix: alkali-activated slag cement (AASC), which is a kind of cementitious material prepared by alkali-activator and pozzolanic or latent hydraulic material. Firstly, the mix ratio of the AASC was optimized to improve the wettability and mechanical properties. Then, the effects of the adhesive matrix and the type of fiber-reinforced polymer (FRP) were observed through FRP-to-concrete bond tests on 93 specimens. The test results, coupled with anchorage analysis, indicate that the AASC has comparable reinforcing effects as those of organic epoxy matrix; the anchorage length of FRP sheets has a significant influence on the failure behavior and failure mode of FRP-enhanced concrete structures. In addition, our tests prove that the AASC has favorable high-temperature resistance and bonding effects. The research results provide a good reference for the design and application of inorganic matrix for FRP-enhancement of concrete structures.

1. Introduction

In recent years, fiber reinforced polymer (FRP) composites have been widely applied to enhance the strength and stiffness of structures, thanks to their ease of handling, superior corrosion resistance, high specific strength, high-temperature resistance. The FRP-reinforced bridges, tunnel linings and

---

buildings are living proof of the remarkable efficiency of the FRP bonding technique [1,2].

The effects of FRP reinforcement directly depend on the adhesive matrix. Organic epoxy matrices, which are commercially available, have often been adopted for FRP reinforcement [3,4]. However, there are several defects with organic matrices, namely, poor resistance to heat and fire, low glass transition temperature T_g (60–82 °C), susceptibility to ultraviolet (UV) radiation, and inapplicability to humid surfaces [5,6].

The above defects can be overcome by an emerging cementitious material: the alkali-activated slag cement (AASC). The AASC was prepared by mixing ground-granulated blast-furnace slag (GGBFS) with alkaline activators [7,8]. This low-viscosity inorganic matrix can effectively penetrate into FRP sheets. Compared with organic epoxy matrices, the AASC is highly resistant to fire and high temperature (its strength at 600 °C is no weaker than that at room temperature), not susceptible to UV radiation, and applicable at low temperatures or on wet surfaces [9,10].

The application of organic matrices is detailed in the *Guide for the Design and Construction of Externally Bonded FRP Systems for Strengthening Concrete Structures*, which is reported by ACI Committee 440 [5]. By contrast, the reinforcement effect of inorganic matrices is only discussed by a few scholars [11–13]. Most studies related to the AASC have only focused on the immobilization of hazardous wastes [14]. There is little report on the performance of concrete structures enhanced with FRP sheets bonded by inorganic matrices rather than organic epoxy matrices [15,16].

This paper attempted to develop a high-temperature resistant inorganic matrix to be an alternative for organic epoxy. For this purpose, the mix ratio of the AASC and type of FRP sheets were optimized in turn. The feasibility of the AASC with the optimal mix ratio, coupled with the best type of FRP sheets, was verified through tests on failure modes, basic anchorage lengths, and strain development at FRP rupture. The research results provide a good reference for the design and application of inorganic matrix for FRP-enhancement of concrete structures.

2. Preparation of AASC

2.1. Materials

The granulated blast furnace slag was grounded in a Vertical Slag Ball Mill to the specific surface area (SSA) of 475 m^2/kg, which fall to Grade S95 specified in the *Ground Granulated Blast Furnace Slag Used for Cement and Concrete* (GB/T 18046-2008). The chemical composition of the GGBFS is explained in Table 1.

The alkaline activator was prepared by mixing sodium hydroxide with potassium silicate. The sodium hydroxide was dissolved in potassium silicate to adjust the modulus (Ms). Firstly, the sodium hydroxide was mixed for about 1 min at low speed, then water was poured into the pan and stirred for approximately 6 min until the mixture was well combined. The potassium silicate belongs to Class 1 as specified in the *Potassium Silicate for Industrial Use* (HG/T 4131-2010), whose specific gravity is 1.465 and silica modulus (Ms_1) is 1.76 ($Ms_1 = SiO_2/K_2O$; $K_2O = 15.98\%$;

Table 1 Chemical composition of the GGBFS.

Name of component	Weight percent
Silica (SiO_2)	33.70
Alumina (Al_2O_3)	14.40
Calcium oxide (CaO)	41.70
Ferrous oxide (FeO)	0.37
Potassium oxide (K_2O)	0.31
Magnesium oxide (MgO)	8.60
Sulphur trioxide (SO_3)	0.40
Sodium oxide (Na_2O)	0.02
Chloride	0.01
Residuum	0.10
Loss on ignition (LOI)	0.39
Specific gravity	2.87 g/cm^3

$SiO_2 = 28.15\%$). The sodium hydroxide pearls were dissolved in potassium silicate solution to adjust its silica modulus ($Ms = SiO_2/(K_2O + Na_2O)$).

2.2. Optimization of mix ratio

To optimize the mix ratio of the AASC for FRP reinforcement, this section investigates the three factors that affect strength and wettability: silica modulus (Ms), sodium silicate-to-slag ratio, and water-to-slag ratio (Table 2).

According to the *Standard for test method of basic properties of construction mortar* (*JGJ/T70-2009*), the compressive strength of the mixture must surpass 70 MPa. For the safety and reliability of the bonding interface, the adhesives should outperform the concrete substrate in mechanical properties [17]. Therefore, based upon *JGJ/T70-2009*, the compressive strength of the AASC at room temperature was tested on an automatic bending compression test and control system (Fig. 1), such as to optimize the mix ratio of the AASC.

In order to more clearly describe the equipment and systems, the specific details are as follows: Firstly, the 40 mm × 40 mm × 160 mm specimen was folded into two halves on the Yaw-300 Automatic Press and Folding Test Machine, and the loading rate of the testing machine was 0.25kN/s. Then, the half specimen (its size was about 40 mm × 40 mm × 80 mm) was pressed in the two sides of the specimen when it was formed. The standard compression fixture could ensure that the compression surface was 40 mm × 40 mm.

The test results [18,19] show that reasonable choice of alkaline activator can make the compressive strength of the mixture surpass 70 MPa. At the same dose, water glass (which means potassium silicate) is the strongest alkaline activator, followed in turn by sodium hydroxide and P.O 42.5 cement. The same dose of water glass and sodium hydroxide can create a more alkaline environment than cement, which is favorable for the hydration of cementitious materials. The superiority of water glass over sodium hydroxide is attributable to Si (OH)$_4$, the hydrolysate of water glass, exists as colloid. During the hydration of water glass, Si(OH)$_4$ can adsorb Si-O anionic group and alkali metal ions in the liquid, resulting in the poly-condensation of monomers and speeding up hydration. The hydrolysate also prevents the Si-O anionic group from super-saturation around slags, and thus depolymerizes the slags.
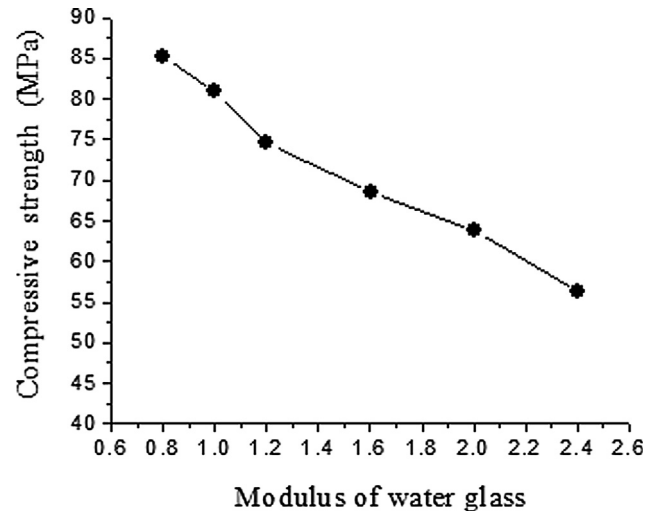
Table 2 The mix ratio of the AASC.

Number	Slag	Silica modulus (Ms)	Potassium silicate amount, %	Sodium hydroxide,%	Water amount %
W32	1	1.0	14	4.58	32
W35	1	1.0	12	5.35	35
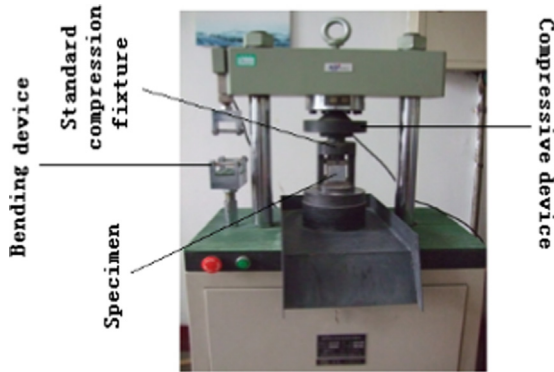
Fig. 1 The automatic bending compression test and control system.

Fig. 2 The effects of modulus of water glass on compressive strength of AASC.

Therefore, potash water glass was adopted as the alkaline activator of the GGBFS. Equal mass of slag (800 g) was employed each time, such as to convert the doses of water glass and water into percentages of slag mass. Three AASC specimens of the size 40 mm × 40 mm × 160 mm were molded and solidified in a standard curing room, and demolded after 24 h after casting. After 28 days of aging, the compressive strength of each specimen was measured as per the *Method of Testing Cements: Determination of Strength* (GB/T 17671-1999).

During the measurement [7,8], the modulus of water glass (The molecular formulas of water glass are $Na_2O \cdot nSiO_2$ and $K_2O \cdot nSiO_2$. The coefficient n in the formula is called the modulus of water glass, which is the molecular ratio (or molar ratio) of silica and alkali metal oxides in water glass) was adjusted from 0.8 to 2.4 by adding a suitable amount of sodium hydroxide. For example, the modulus of water glass M = 1.0 was achieved by adjusting the molar ratio of the solution to $n(SiO_2):m(K_2O + Na_2O) = 1.0:1$. As shown in Fig. 2, the compressive strength of 40 mm × 40 mm × 160 mm specimen was decreased with the growing modulus of water glass. When the modulus was M = 0.8, the water glass became viscous and virtually immobile; a small amount of crystalline precipitated after standing for a while at room temperature. Once the modulus increased to M = 1.0, the mobility of the water glass was relatively good, leaving no sign of crystallization; meanwhile, the compressive strength of the specimens could reach 80.88 MPa. Therefore, the modulus of water glass is set to 1.0 in this research.

Under the modulus of water glass of 1.0, the dose of water glass was increased from 8% to 22%. The results of 40 mm × 40 mm × 160 mm specimen in Table 3 and Fig. 3 show that, the compressive strength of AASC first increased and then decreased, with the growing dose of water glass. Hence, there must be an optimal range for the dose of water glass. If the dose is too small, the hydration cannot proceed thoroughly, failing to fully activate the slags; if the dose is too large, the excess alkalis will react with CO_2 in the air to produce carbonates, which suppresses the compressive strength of the cementitious material. What is worse, the heavy presence of hydroxyl radicals will lead to a rapid accumulation of hydrates around slag particles, forming a protective film that prevents further reaction and delays the strength development of the cementitious material. Therefore, the dose of water glass is set to 12% in this research.

Furthermore, the compressive strength of each specimen was measured, as the dose of water (part of which comes from the water glass) was changed from 35%, 42% to 45%. It can be seen from the measured results of 40 mm × 40 mm × 160 mm specimen (Fig. 4) that, at the water dose of 35%, the compressive strength of AASC reached 90.16 MPa. In this case, the adhesive was relatively viscous, and the initial setting time was merely 30 min, failing to meet the time requirements of construction operations. At the water dose of 42%, the compressive strength of the AASC stood at 80.88 MPa, and the adhesive was moderately viscous. In this case, the initial and final setting times of AASC were 45 min and 80 min, respectively. Thus, the FRP sheets could be fully infiltrated and pestled to complete the paste operation. At the water dose of 45%, the adhesive had relatively poor cohesion, and the AASC exhibited relatively low compressive strength. As a result, the water dose was set to 42% for further analysis.

## 3. FRP-to-concrete bond tests at room temperature

3.1. Test materials

Besides the mix ratio of AASC, the bonding between AASC and FRP sheets in reinforcement of concrete structures was

Table 3 The effects of dose of water glass on compressive strength of AASC (MPa).

Dose of water glass	Compressive strength						Mean strength
	1	2	3	4	5	6	
8%	70.69	69.86	71.05	69.51	70.94	71.49	70.59
10%	74.80	75.16	76.01	75.37	76.23	76.51	75.68
12%	80.91	80.58	80.63	81.22	81.19	80.75	80.88
14%	78.19	77.75	78.44	77.90	76.58	76.74	77.60
16%	73.68	74.19	74.63	74.01	74.14	74.37	74.17
18%	69.33	70.94	69.85	70.75	71.19	70.64	70.45
20%	54.19	54.27	54.56	55.04	54.20	54.14	54.40
22%	46.97	47.45	47.33	47.85	47.20	47.78	47.43

Note: (a) The AASC specimens were of the size 40 mm × 40 mm × 160 mm; (b) As shown in Fig. 1, each specimen was split into two halves along the centerline with a bending device, and one half was crushed with one side facing up in the standard compression fixture; (c) The standard compression fixture has a bearing plate, which controls the compression area as a 40 mm × 40 mm square.
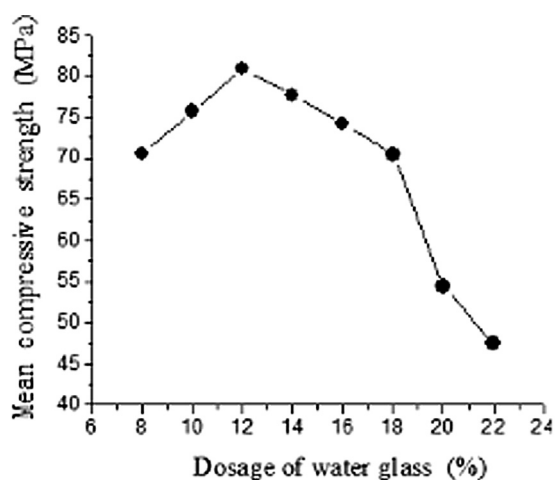
Fig. 3 The effects of dosage of water glass on compressive strength of AASC.
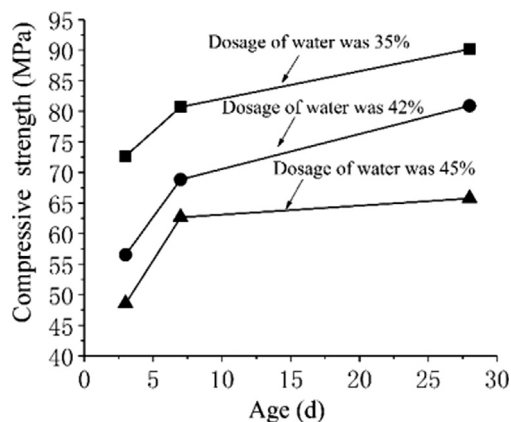
Fig. 4 The effects of dosage of water on compressive strength of AASC.

also affected by the tensile strength and wettability of FRP sheets. Hence, three kinds of FRP sheets were subjected to double shear tests, including UT70-20 carbon fiber reinforced polymer (CFRP) sheets (Toray, Japan), UT70-30 CFRP sheets (Toray, Japan), and BUF13-380 basalt fiber reinforced polymer (BFRP) sheets (Zhejiang Goldstone Co., China). Table 4 lists the basic properties of the three FRP sheets.

Before the FRP-to-concrete bond tests, the AASC specimens were prepared with the optimized mix ratio, and concrete blocks (size: 100 mm × 100 mm × 100 mm) were enhanced with one layer of FRP sheet (width: 70 mm; length: 100 mm) bonded with AASC for in-plane shear tests. Three standard concrete blocks (size: 150 mm × 150 mm × 150 mm) were casted for unconfined compressive strength tests, according to the *Code for Design of Concrete Structures*. The compressive strength of these blocks was 31.55 MPa at the age of 28 days.

3.2. Test procedure

According to the *Technical Specification for Strengthening Concrete Structures with* Carbon Fiber *Reinforced Polymer Laminate* (CECS 146: 2003), the test procedure was designed as follows (Fig. 5), with the same ratio of AASC serving as the primer, putty and saturant.

Step 1. Cleaning the surface of concrete

To create a good bonding layer, the structural layer of the concrete should be exposed. Therefore, the concrete surface was polished smooth, and rid of any loose surface material. To enhance the bond between FRP sheets and concrete, the dusts, oil stains and other impurities were erased from the concrete surface with acetone. The cleaned surface was kept wet before applying the FRP sheets.

Step 2. Clipping the FRP sheets

To meet the test requirements, the FRP sheets were clipped into strips 600 mm in length and 70 mm in width.

Step 3. Impregnating and pestling the FRP strips

The FRP strips were immersed in a square groove filled with AASC prepared with the optimal mix ratio, and then pestled unidirectionally with a smooth roller for 15 min.
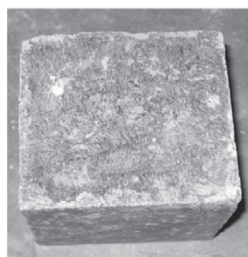
Step 4. Brushing the primer

The AASC was brushed uniformly onto the concrete surface, and the adhesive was controlled within 2 mm thick.

Table 4 The basic properties of the three FRP sheets.

| Type	Ma (g/m²)	t_f (mm)	T (MPa)	E (GPa)	δ (%)
UT70-20 CFRP sheets	200	0.111	4114	243	1.71
UT70-30 CFRP sheets	300	0.167	4125	244	1.71
BUF13-380 BFRP sheets	380	0.180	2300	91	2.60

Note: Ma is mass per unit area; t_f is calculated thickness; T is standard tensile strength; E is elastic modulus; δ is elongation under sustained loading.
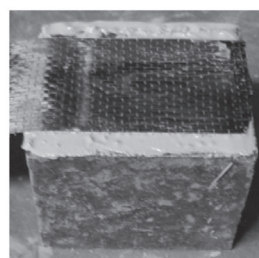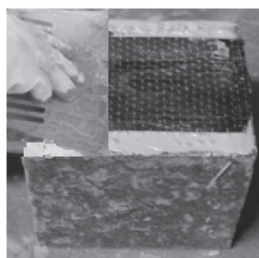

(a) Cleaning the surface of concrete.

(b) Impregnating and pestling the FRP strips.
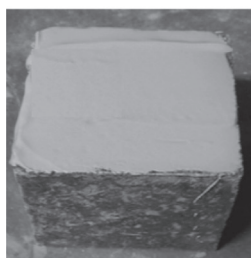
(c) Brushing the primer.

(d) Bonding the FRP strips.

(e) Expelling the air bubbles.

(f) Brushing the surface adhesive.

Fig. 5 The bonding of the FRP sheets.

Step 5. Bonding the FRP strips

Each impregnated and pestled FRP strip was pasted on the concrete surface (droplet side down). Then, the air bubbles within the AASC were expelled with a plastic scraper.

Step 6. Brushing the surface adhesive

The AASC was brushed uniformly onto the surface of the externally bonded FRP strips, guarding against potentially damaging environmental and mechanical effects. The adhesive was controlled within 2 mm thick.

Step 7. Specimen curing

The bonded specimens were solidified in a standard curing room until 3d, 7d and 28d age.

Step 8. Double shear testing

A total of 33 concrete cubes with 100 mm × 100 mm × 100 mm size were reinforced with FRP sheets bonded with AASC or organic adhesive, and subjected to double shear tests (Fig. 6).

3.3. Comparison of bonding effects of FRP sheets

Theoretically, there are four typical failure modes for FRP sheets bonded to concrete blocks with inorganic matrices: test [1]: concrete failure, test [2]: concrete-to-adhesive interface failure, test [3]: adhesive failure, and test [4]: FRP-to-adhesive interface failure. After concrete failure, a large area of concrete adjacent to the adhesive-concrete interface will cling to the FRP strip; after concrete-to-adhesive interface failure, the entire adhesive layer and a few concrete will cling to the

FRP strip; after adhesive failure, the concrete will be separated from the FRP strip, as the adhesive layer slips internally; after FRP-to-adhesive interface failure, most adhesives will cling to the concrete surface.

For the above four failure modes, the tensile strength of the adhesive should be much greater than that of concrete, if there is a good wettability between the adhesive and FRP sheets. The latter three failure modes rarely appear in reliable constructions, and should not appear in concrete structures reinforced with FRP sheets. Hence, the ideal failure mode is concrete failure, after which a thin layer of concrete is peeled off from the concrete surface.

The mechanical model of the in-plane shear test is shown in Fig. 7, where t_a is the primer thickness (about 2 mm); t_f is the calculated thickness of single-layer FRP sheet (about 0–0.2 mm); b_c is the width of concrete specimens (about 100 mm); b_f is the width of single-layer FRP sheet (about 0–100 mm); L_a is the anchorage length of FRP sheets (about 200–500 mm) [20–23].

Fig. 8 displays the failure situations of the concrete specimens enhanced with each of the three FRP sheets bonded with AASC. Table 5 compares the in-plane shear strengths of the three FRP sheets at different ages.

The comparison shows that the UT70-20 CFRP sheets, which are relatively thin, suffered both peeling and tensile failure during the double shear tests; the UT70-30 CFRP sheets, which are moderately dense, were stripped as a whole plate through impregnating and pestling in the AASC; the BUF13-380 BFRP sheets, which have poor wettability, showed a small in-plane shear strength; after failure, some adhesives were attached to the concrete reinforced with BFRP sheets. Thus, the UT70-20 and UT70-30 CFRP sheets bonded with AASC can effectively reinforce the concrete specimens.
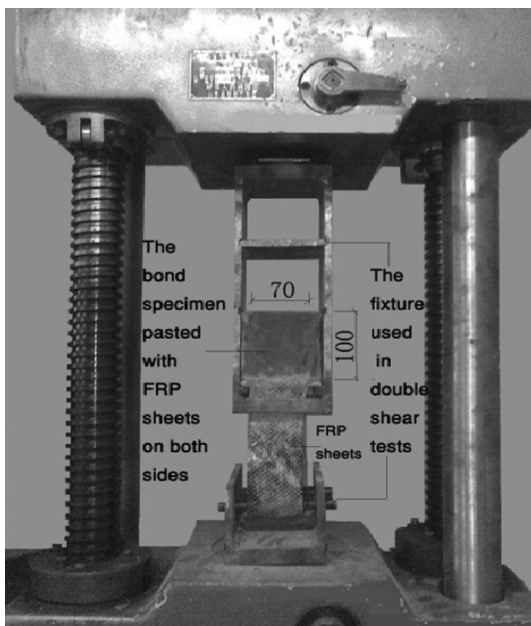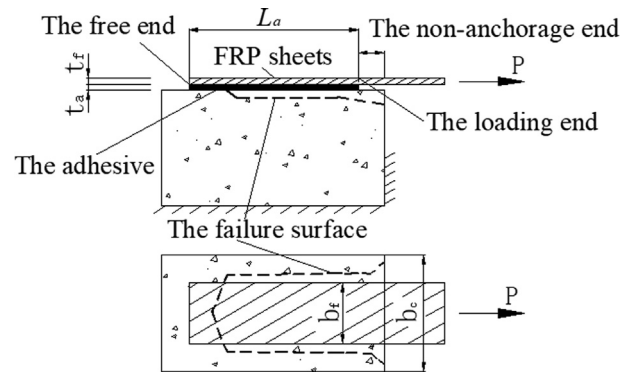

Fig. 7   The mechanical model of in-plane shear test [1].

3.4. Comparison of shear effects between AASC and organic adhesive

The CFRP sheets separately bonded with the AASC and organic epoxy were subjected to double shear tests. The tensile strengths of the two types of sheets were both above 3.5 MPa, greater than the tensile strength of concrete. The specimen size and preparation procedure were mentioned in Section 2.1 and the failure situations are displayed in Fig. 9. The test results are listed in Table 6.

It can be seen that the CFRP sheets bonded with AASC achieved an in-plane shear strength of 1.34 MPa, which was almost the same as that of those bonded with organic epoxy. Moreover, these CFRP sheets brought the ideal failure mode: a large area of concrete adjacent to the adhesive-concrete interface clung to the FRP strip. The comparison proves the feasibility of reinforcing concrete structures with FRP sheets bonded with AASC.

4. CFRP anchorage length tests at room temperature

The synergy between CFRP sheets and concrete depends on the bonding strength of the interfaces between the CFRP sheets, the adhesive and the concrete. To maximize the enhancing effect of the CFRP sheets, the interface must have sufficient bonding strength to transfer shear stress. If the anchorage length of CFRP sheets is insufficient, the stress will concentrate on the CFRP end, causing the FRP strip to detach from the concrete. In this case, the CFRP sheets will cease to exert the enhancing effect. If the anchorage length of CFRP sheets is too long, there will be a huge waste of materials. Therefore, the anchorage length must be properly determined in practical engineering [16].

4.1. Test program

Under flexural stress, the height of the reinforced concrete beams is much greater than the thickness of CFRP sheets. Hence, the reinforced concrete beams may have to bear all the vertical shear stress. Meanwhile, the CFRP sheets anchored to the bottom of the beam mainly withstand the interfacial shear stress, and the effect of normal peeling stress is so small as to be negligible. As a result, the basic anchorage length of CFRP sheets was identified through a double shear test, which saves labor and raw materials.
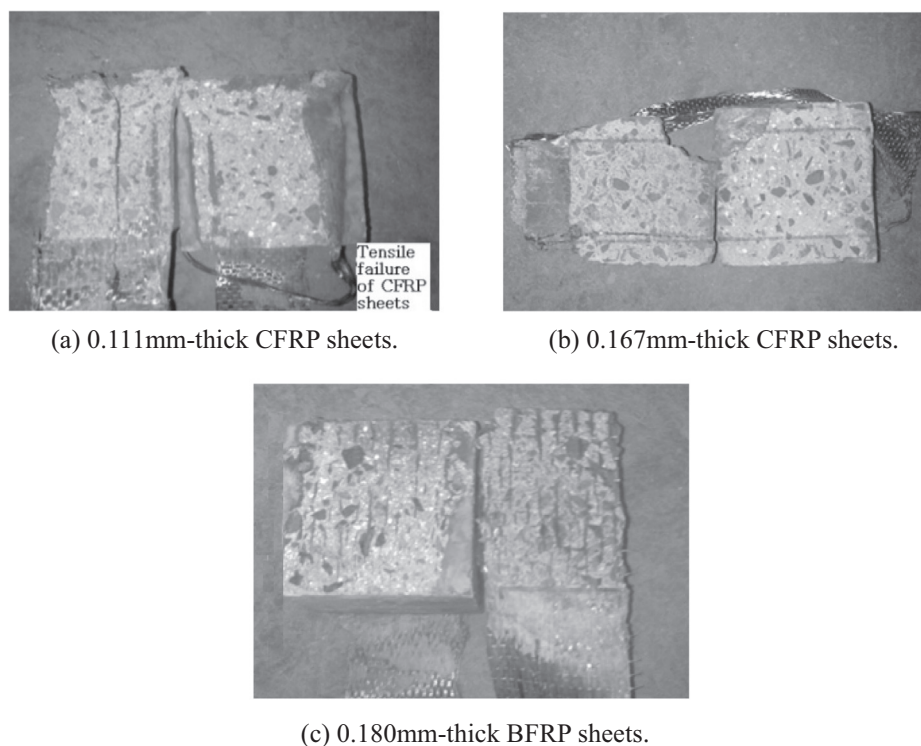

Fig. 6   The instrument of double-shear tests.

(a) 0.111mm-thick CFRP sheets.

(b) 0.167mm-thick CFRP sheets.

(c) 0.180mm-thick BFRP sheets.

Fig. 8 The failure situations of the concrete specimens enhanced with each of the three FRP sheets bonded with AASC.

A total of 10 concrete samples were reinforced with CFRP sheets bonded with AASC, and subjected to double shear tests. Both UT70-20 and UT70-30 CFRP sheets were selected for the double shear test, in addition to a concrete prism of the size 1,000 mm × 160 mm × 160 mm. The concrete surface was bonded with one layer of 70 mm-width CFRP sheets. The materials were prepared as mentioned in Section 2.1, and the test instrument is illustrated in Fig. 10. To ensure the enhancing effect, four reinforcing steel bars (diameter: 12 mm) were embedded in each concrete prism. The distance from the concrete surface to the outside of the stirrups (diameter: 6 mm) was 25 mm. The stirrups were arranged at an interval of 150 mm. The mechanical properties of the steel bars are listed in Table 7.

Assuming that the bonding stress is uniformly distributed along the anchorage length of CFRP sheets, the average shear strength can be calculated by:

$$\tau = \frac{\bar{P}}{2b_f L_a} \tag{1}$$

where, τ is the mean shear strength; $\bar{P}$ is the mean failure load; b_f is the width of the CFRP strip; L_a is the anchorage length of the CFRP sheets. Obviously, the mean shear strength is not equal to maximum bond stress. However, the mean shear strength can serve as a reference in the evaluation of bonding strength.

The anchorage lengths of CFRP sheets were identified by changing the bonding length of the CFRP sheets and measuring their strain development [20]. The strain gauges were positioned close to the loading end along the anchorage length at an interval of 10 mm. The center of the first strain gauge was 5 mm from the loading end. The interval between the middle strain gauges was 10 mm, and that between the last three strain gauges was 15 mm.

4.2. Results analysis

As shown in Fig. 11, two anchorage failure modes were observed from 20 specimens: 16 specimens suffered from anchorage failure and 4 underwent tensile failure of CFRP sheets.

(1) Anchorage failure

In 16 specimens, the concrete cover peeled off near the CFRP sheets. The peeling started as visible cracking near the loading end of the concrete prism, along the longitudinal axis of the CFRP sheets. With the growth in external load, the concrete cracking kicked off interfacial peeling of the CFRP strip off the loading end. The peeling mainly occurred in the middle of the specimen along the longitudinal axis. A thin layer of concrete peeled off and clung to the CFRP strip, giving off a loud popping sound. Once the anchorage length was insufficient, the anchorage failure would take place.

(2) Tensile failure of CFRP sheets

In 4 specimens, a crisp sound was heard due to the peeling of concrete adjacent to the adhesive-concrete surface, when the external load grew to about 80% of the ultimate load. This means the CFRP sheets were pulled uniformly. Then, a sharp crackling sound might be heard due to CFRP rupture. The fractured surface of the CFRP sheets generally had zigzagging cracks, and concentrated in the non-anchorage zone of CFRP

Table 5 Comparison of the in-plane shear strengths of three FRP sheets.

Type	t_f (mm)	A (d)	No.	P (kN)	Failure mode	R (%)	$\bar{P}$ (kN)	τ (MPa)
UT70-20 CFRP sheets	0.111	3	1	12.0		60%	13.27	≥0.95
			2	13.3	Failure mode (1)	70%		
			3	14.5		75%		
		7	1	13.2		80%	14.40	≥1.03
			2	14.7	Failure mode (1)	75%		
			3	15.3		80%		
		28	1	15.8		75%	16.87	≥1.20
			2	16.5	Failure mode (1)	85%		
			3	18.3		90%		
UT70-30 CFRP sheets	0.167	3	1	14.4		30%	15.43	1.12
			2	15.6	Failure mode (1)	45%		
			3	16.3		60%		
		7	1	16.4		70%	18.10	1.29
			2	18.6	Failure mode (1)	75%		
			3	19.3		85%		
		28	1	17.7		80%	18.70	1.34
			2	18.1	Failure mode (1)	85%		
			3	20.3		95%		
BUF13-380 BFRP sheets	0.180	3	1	8.7	Failure mode (1)	30%	9.03	0.65
			2	9.1	Failure mode (4)	—		
			3	9.3	Failure mode (4)	—		
		7	1	10.6	Failure mode (1)	65%	10.83	0.77
			2	10.7	Failure mode (4)	—		
			3	11.2	Failure mode (1)	70%		
		28	1	10.9	Failure mode (1)	80%	11.57	0.83
			2	11.7	Failure mode (4)	—		
			3	12.1	Failure mode (1)	85%		

Note: t_f is calculated thickness; A is age; No. is number of specimen; P is failure load; $\bar{P}$ is mean failure load; τ is mean shear strength; R is the peeling area ratio, i.e. the ratio of the peeling area of concrete to the bonding area of FRP sheets (A_c/A_f) measured by the coordinate paper; — means no concrete peeled off; ≥ means the actual shear strength is no less than the listed value, due to the coexistence of peeling and tensile failure of 0.111 m-thick CFRP sheets.
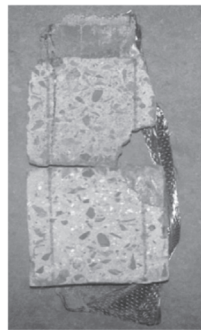
(a) 0.167mm-thick CFRP sheets bonded with AASC.
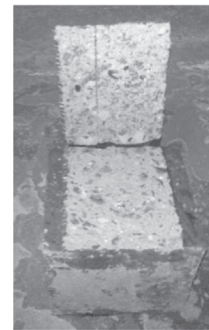
(b) 0.167mm-thick CFRP sheets bonded with organic epoxy.

Fig. 9 The failure situations of the CFRP sheets separately bonded with the AASC and organic epoxy.

sheets. Once the anchorage length was insufficient, the CFRP sheets would suffer from tensile failure.

The anchorage length of CFRP sheets could be identified clearly based on the test results in Table 8. This explains precisely the concept of anchorage length: the length along the CFRP sheets that the stress is transferred, i.e. the length along the CFRP sheets with non-zero strain.
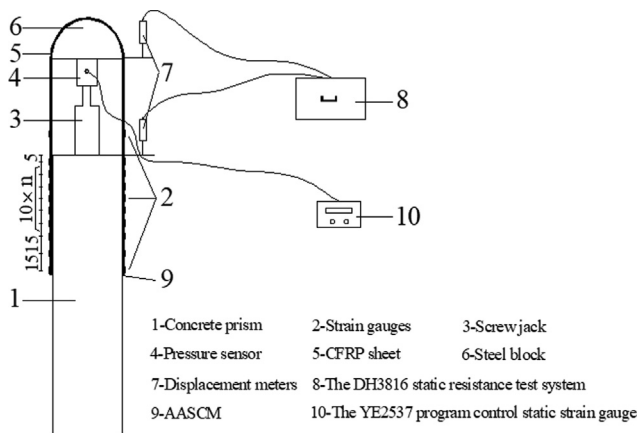
From the Fig. 11, it is proved that when the anchorage length of CFRP sheet is not enough, the specimen suffers from anchorage failure. When the anchorage length of CFRP sheet is enough, the specimen suffers from tensile failure of CFRP sheet.

Fig. 12 shows the strain distribution and development for specimens T-10 and T-20 along the CFRP strip, where P is the applied load; P_u is the ultimate load; s is the slip at the loaded end. It can be seen that the anchorage length increased almost linearly with the applied load, but the mean shear strength decreased with the growing anchorage length

Table 6 Comparison of in-plane shear strengths between AASC and organic epoxy.

Type	t_f (mm)	Adhesive	No.	P (kN)	Failure mode	R (%)	$\bar{P}$ (kN)	τ (MPa)
UT70-20 CFRP sheets	0.111	AASC	1	15.8		75%	16.87	1.20
			2	16.5	Failure mode (1)	85%		
			3	18.3		90%		
		Organic epoxy	1	15.9		85%	16.67	1.19
			2	18.1	Failure mode (1)	90%		
			3	16.0		95%		
UT70-30 CFRP sheets	0.167	AASC	1	17.7		80%	18.70	1.34
			2	18.1	Failure mode (1)	85%		
			3	20.3		95%		
		Organic epoxy	1	18.1		85%	18.68	1.33
			2	18.6	Failure mode (1)	95%		
			3	19.3		100%		

Fig. 10 The sketch map of the test instrument.

1-Concrete prism   2-Strain gauges   3-Screw jack
4-Pressure sensor   5-CFRP sheet   6-Steel block
7-Displacement meters   8-The DH3816 static resistance test system
9-AASCM   10-The YE2537 program control static strain gauge

Table 7 The mechanical properties of the steel bars.

Reinforcing bars	Yield strength fy (MPa)	Ultimate strength fu (MPa)	Young's modulus E_s (GPa)
D12	358.83	533.75	163
D6	278.21	431.54	184

(Table 8). According to the strain development along the length of the CFRP sheets, it is clear that the CFRP sheets did not reach their fracture strains. Consequently, the basic anchorage length is negatively correlated with the length of the high stress area (the strain of CFRP sheet is higher as shown in Fig. 1).

As shown in Table 8, when grade C30 concrete specimens are strengthened with CFRP sheets bonded with AASC, the test results show that strains measurement of CFRP approach zero in 200 mm and 300 mm. Therefore, the basic anchorage length of 0.111 mm-thick CFRP sheets should be greater than

200 mm, and that of 0.167 mm-thick CFRP sheets should be greater than 300 mm.

5. Bonding performance at high temperature

5.1. Test method

A total of 10 concrete samples were reinforced with CFRP sheets bonded with AASC, and subjected to double shear tests. The anchorage length was adjusted from 225 mm to 400 mm. The high temperature tests were performed at six different target temperatures: 20 °C, 100 °C, 200 °C, 300 °C, 400 °C, 500 °C in an electric furnace (Fig. 13). 4 °C/min was set as the heating rate. When the temperature inside furnace reached the target temperature, the constant temperature time was 2 h to make the specimens temperature homogenous. The specimens were then cooled down to room temperature naturally in furnace. Finally, the specimens were taken out from the furnace and each of the symmetrical sides of the specimen was pasted with strain gauges. Stain gauges and displacement sensors were used to measure strains in the CFRP sheets and displacements at various positions, as shown in Fig. 10.

5.2. Result analysis at high temperature

The temperature holding time was measured by thermocouples embedded in AASC specimen at 4 mm to the surface (Fig. 14). The furnace temperature and measured temperatures are displayed in Fig. 15. It can be seen that the temperature holding time was 30 min.

The two anchorage failure modes were observed as the temperature increased at the heating rate of 4 °C/min from 100 °C to 500 °C. The test phenomena are presented in Fig. 16 below.

When the temperature increased from 100 °C to 500 °C, the anchorage lengths were measured as 387.5 mm (at 100 °C), 337.5 mm (at 200 °C), 312.5 mm (at 300 °C), 300 mm (at 400 °C) and 300 mm (at 500 °C), respectively. The measured values were compared with the anchorage length at room temperature to reveal the change law of CFRP anchorage length with temperature by using the formula (2) below:

$$\frac{L_{a.T}}{L_a} = \begin{cases} 0.91 + 4.80\left(\frac{T}{1000}\right) & 20\,^{\circ}\text{C} \leqslant T \leqslant 100\,^{\circ}\text{C}, & R^2 = 0.999 \\ 1.73 - 4.53\left(\frac{T}{1000}\right) + 11.65\left(\frac{T}{1000}\right)^2 - 11.17\left(\frac{T}{1000}\right)^3 & 100\,^{\circ}\text{C} < T \leqslant 500\,^{\circ}\text{C}, & R^2 = 0.997 \end{cases} \tag{2}$$

where, $L_{a.T}$ is the anchorage length of the CFRP sheets at temperature T (mm); L_a is the anchorage length of the CFRP sheets at room temperature (20 °C) (mm); T is the current temperature (°C); R^2 is the correlation coefficient of fitting accuracy.

Fig. 17 compares the fitted curve obtained by formula (2) and the test curve. It can be seen that the anchorage lengths of CFRP sheets increased from 280 mm to 387.5 mm, as the temperature rose from 20 °C to 100 °C, and decreased from 387.5 mm to 275 mm as the temperature climbed from
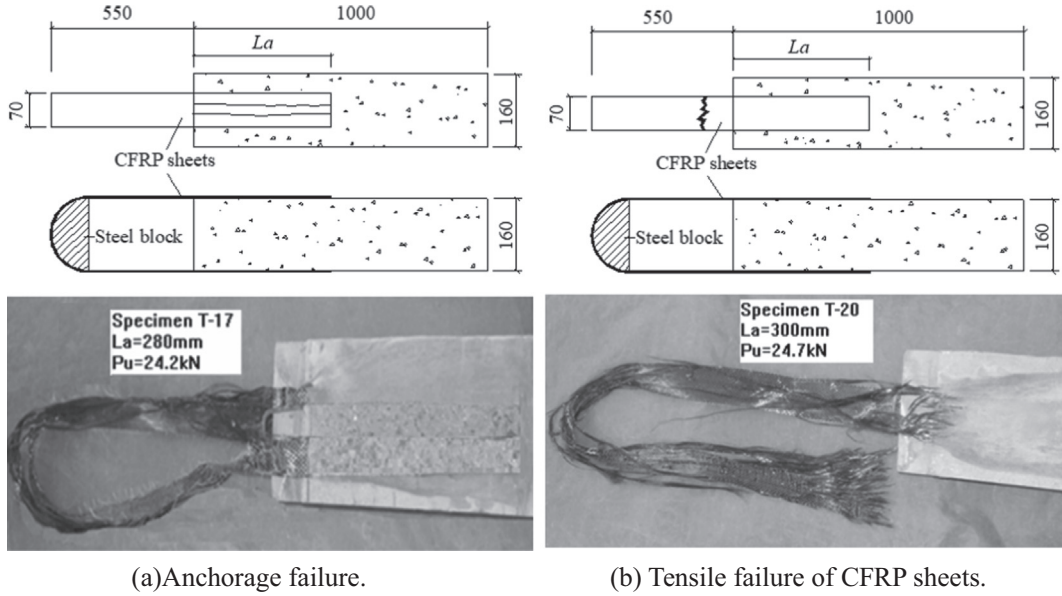

(a) Anchorage failure.

(b) Tensile failure of CFRP sheets.

Fig. 11   The anchorage failure modes.

Table 8   The test results on the anchorage length of CFRP sheets.

Type	t_f (mm)	No.	L_a (mm)	P (kN)	Anchorage failure modes	R (%)	$\bar{P}$ (kN)	τ (MPa)
UT70-20	0.111	T-1	120	16.9	AF	95%	17.20	1.02
CFRP sheets		T-2		17.5		80%		
		T-3	140	18.4	AF	75%	18.25	0.93
		T-4		18.1		80%		
		T-5	160	18.8	AF	65%	19.01	0.85
		T-6		19.2		85%		
		T-7	180	19.7	AF	45%	19.55	0.78
		T-8		19.4		30%		
		T-9	200	19.8	CR	—	19.95	0.71
		T-10		20.1		—		
UT70-30	0.167	T-11	220	20.8	AF	80%	21.05	0.68
CFRP sheets		T-12		21.3		75%		
		T-13	240	21.9		65%	22.20	0.66
		T-14		22.5	AF	70%		
		T-15	260	23.4		45%	23.65	0.65
		T-16		23.9	AF	30%		
		T-17	280	24.2		30%	24.00	0.61
		T-18		23.8	AF	35%		
		T-19	300	24.0	CR	—	24.35	0.58
		T-20		24.7		—		

Note: AF is anchorage failure; CR is CFRP rupture.
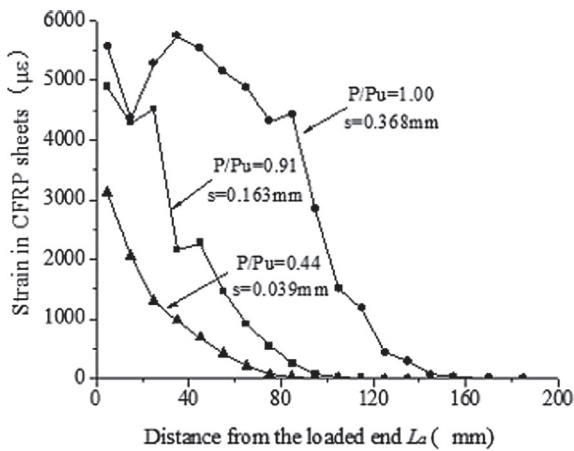
(a) Strain development along 0.111mm-thick
CFRP sheets for specimen T-10: L_a=200mm.

Fig. 14   Specimens with thermocouples.
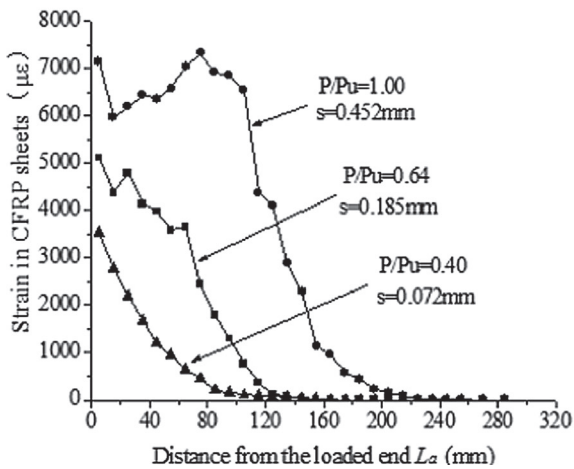
(b) Strain development along 0.167mm-thick
CFRP sheets for specimen T-20: L_a=300mm.

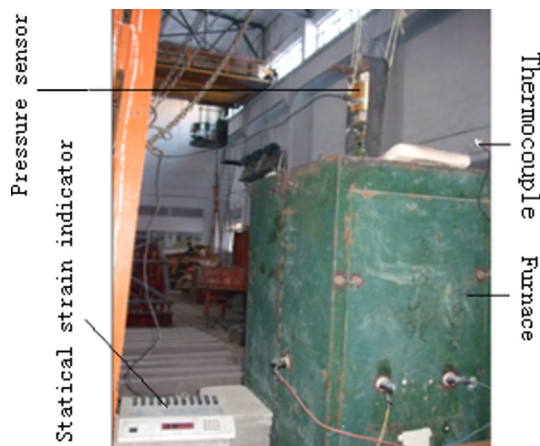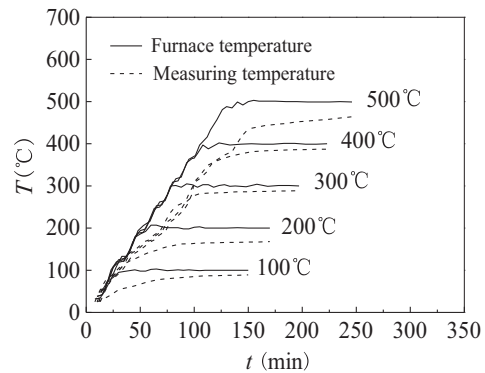**Fig. 12**   Strain development along the length of CFRP sheets.

Fig. 15   Furnace temperature and measured temperatures.

100 °C to 500 °C. In short, basic anchorage lengths at high temperature were higher than those at room temperature.

5.3. Result analysis after high temperature

When target temperatures are 100–500 °C after high temperature, the anchorage lengths were measured as 487.5 mm, 475 mm and 450 mm, 437.5 mm and 400 mm, respectively. Comparative analysis shows that the double shear specimens after high temperature were the same as those under ambient temperature. However, the colors of AASC and concrete faded, and concrete stripping areas after high temperature were bigger than those at room temperature.

Compared with those under high temperature, the double shear specimens after high temperature witnessed a large area of concrete stripping. Obviously, the AASC provides the anaerobic protection for CFRP after high temperature and at high temperature, preventing the latter from being oxidized. The CFRP anchor lengths after high temperature were fitted from those at high temperature by:

Fig. 13   The sketch map of the test instrument at high temperature.

$$\frac{L'_{a.T}}{L_a} = \begin{cases} 0.82 + 9.26\left(\frac{T}{1000}\right) & 20\ ^\circ C \leq T \leq 100\ ^\circ C,\ R^2 = 0.999 \\ 1.83 - 1.09\left(\frac{T}{1000}\right) & 100\ ^\circ C < T \leq 500\ ^\circ C,\ R^2 = 0.988 \end{cases}$$

(3)

(a) Anchorage failure.   (b) Tensile failure of CFRP sheets.
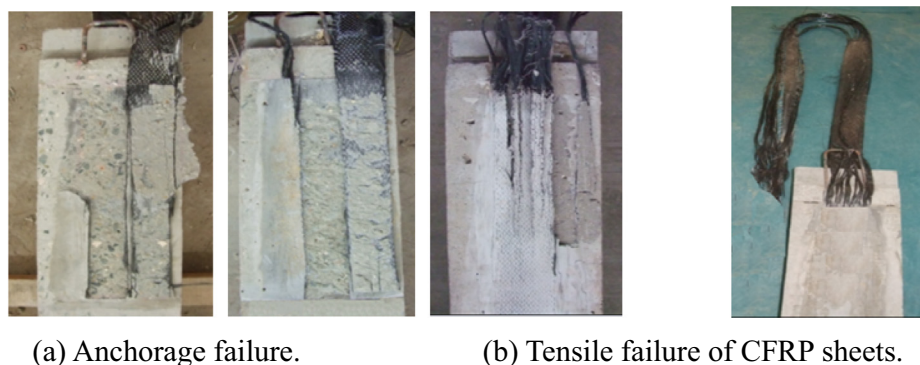
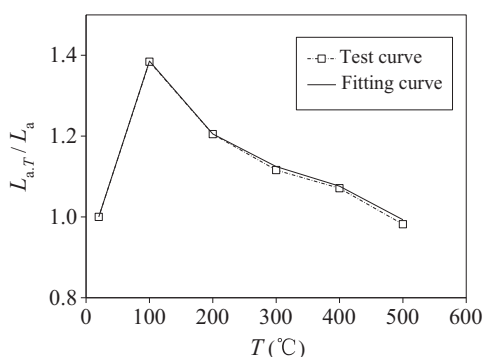**Fig. 16**   The anchorage failure modes at high temperature.

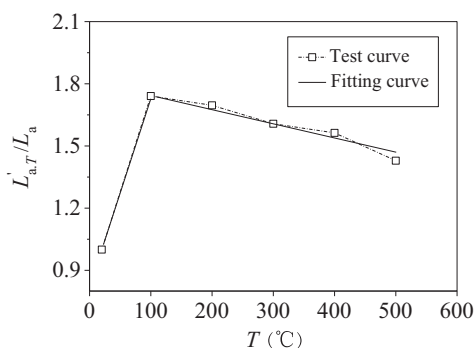**Fig. 17**   The fitted curve and test curve at high temperature.

Fig. 18   The fitted curve and test curve after high temperature.

where, $L'_{a,T}$ is the anchor length of CFRP after temperature T (mm).

Fig. 18 compares the fitted curve obtained by formula (3) and the test curve. It can be seen that the anchorage lengths of CFRP sheets increased linearly from 280 mm to 487.5 mm after the temperature of 20–100 °C, and declined gradually from 487.5 mm to 400 mm after the temperature of 100–500 °C. Hence, the basic anchorage lengths after high temperature were higher than those at room temperature and those at high temperature.

6. Conclusions

This paper presents a high-temperature resistant inorganic matrix: alkali-activated slag cement (AASC), which is expected to become an alternative for organic epoxy. Experimental results show that the modulus of water glass should be around M = 1.0; the dose of water glass and that of water should be around 12% and 42%, respectively. In the considered cases, UT70-30 CFRP sheets achieved the best performance, followed in turn by UT70-20 CFRP sheets and BFRP sheets.

The adhesive matrix directly bears on the bonding between concrete and the FRP sheets. The comparison against organic epoxy matrix shows the feasibility of reinforcing concrete structures with FRP sheets bonded with AASC.

When grade C30 concrete specimens are strengthened with CFRP sheets bonded with AASC, the basic anchorage length of 0.111 mm-thick CFRP sheets should be greater than 200 mm, and that of 0.167 mm-thick CFRP sheets should be greater than 300 mm.

The failure loads and anchorage lengths were measured at high temperature and after high temperature. The basic anchorage lengths of CFRP sheets after high temperature were higher than those at room temperature and those at high temperature. The fitted anchorage length agrees well with the length measured in tests.

The use of AASC as an adhesive is only part of the engineering application, and future work is to probe the AASC as an alternative of concrete or clay.

Declaration of Competing Interest

The authors declare that they have no known competing financial interests or personal relationships that could have appeared to influence the work reported in this paper.

References

[1] C. Carloni, S. Verre, L.H. Sneed, L. Ombres, Loading rate effect on the debonding phenomenon in fiber reinforced cementitious matrix-concrete joints, Compos. B Eng. 108 (2017) 301–314, https://doi.org/10.1016/j.compositesb.2016.09.087.

[2] H.K.R. Komma, R. Nerella, S.R.C. Madduru, Art-of-review on CFRP wrapping to strengthen compressive and flexural behavior of concrete, Revue des Composites et des Matériaux Avancés 29 (3) (2019) 159–163, https://doi.org/10.18280/rcma.290305.

[3] S. Premkumar, C.K. Chozhan, M. Alagar, Studies on thermal, mechanical and morphological behaviour of caprolactam blocked methylenediphenyl diisocyanate toughened bismaleimide modified epoxy matrices, Eur. Polym. J. 44 (8) (2008) 2599–2607, https://doi.org/10.1016/j.eurpolymj.2008.05.031.

[4] J.G. Teng, J.F. Chen, S.T. Smith, L. Lam, FRP Strengthened RC Structures, John Wiley & Sons, UK, 2002, pp. 25–67.

[5] ACI Committee 440. Guide for the Design and Construction of Externally Bonded FRP Systems for Strengthening Concrete Structures, second ed., Farmington Hills, MI, USA, 2008, pp. 2–13.

[6] A.D. Ambrisi, F. Focacci, Flexural strengthening of RC beams with cement-based composites, J. Compos. Constr. 15 (5) (2011) 707–720, https://doi.org/10.1061/(ASCE)CC.1943-5614.0000218.

[7] J. Zhu, W. Zheng, L. Sneed, Y. Huang, C. Xu, Mechanical properties of plant fibers reinforced alkali-activated slag cementitious material at high temperature, Annales de Chimie; Science des Materiaux 43 (4) (2019) 240–255, https://doi.org/10.18280/acsm.430408.

[8] J. Zhu, W. Zheng, L. Xie, Y. Wu, Y. Zhang, J. Fu, Study on the performance of reinforced concrete blocks treated by styrene-acrylic emulsion, Chem. Eng. Trans. 66 (2018) 85–90, https://doi.org/10.3303/CET1866015.

[9] L.H. Sneed, S. Verre, C. Carloni, L. Ombres, Flexural behavior of RC beams strengthened with steel-FRCM composite, Eng. Struct. 127 (2016) 686–699, https://doi.org/10.1016/j.engstruct.2016.09.006.

[10] W. Zheng, J. Zhu, The effect of elevated temperature on bond performance of alkali-activated GGBFS paste, J. Wuhan Univ. Technol. – Mater. Sci. Ed. 28 (4) (2013) 721–725, https://doi.org/10.1007/s11595-013-0759-5.

[11] L.H. Sneed, T. D'Antino, C. Carloni, Investigation of bond behavior of polyparaphenylene benzobisoxazole fiber-reinforced cementitious matrix-concrete interface, ACI Mater. J. 111 (2014) 1–12.

[12] H. Toutanji, L. Zhao, Y. Zhang, Flexural behavior of reinforced concrete beams externally strengthened with CFRP sheets bonded with an inorganic matrix, Eng. Struct. 28 (4) (2006) 557–566, https://doi.org/10.1016/j.engstruct.2005.09.011.

[13] H. Toutanji, Y. Deng, Comparison between organic and inorganic matrices for RC beams strengthened with carbon fiber sheets, J. Compos. Constr. 11 (5) (2007) 507–513, https://doi.org/10.1061/(ASCE)1090-0268(2007)11:5(507).

[14] J. Deja, Immobilization of Cr^{6+}, Cd^{2+}, Zn^{2+} and Pb^{2+} in alkali-activated slag binders, Cem. Concr. Res. 32 (12) (2002) 1971–1979, https://doi.org/10.1016/S0008-8846(02)00904-3.

[15] H. Diab, Z.S. Wu, K. Iwashita, Short and long-term bond performance of prestressed FRP sheet anchorages, Eng. Struct. 31 (5) (2009) 1241–1249, https://doi.org/10.1016/j.engstruct.2009.01.02.

[16] B. Täljsten, Defining anchor lengths of steel and CFRP plates bonded to concrete, Int. J. Adhes. Adhes. 17 (4) (1997) 319–327, https://doi.org/10.1016/S0143-7496(97)00018-3.

[17] S.V. Grelle, L.H. Sneed, Review of anchorage systems for externally bonded FRP laminates, Int. J. Concrete Struct. Mater. 7 (1) (2013) 17–33, https://doi.org/10.1007/s40069-013-0029-0.

[18] A. Fernandez-Jimenezw, A. Palomo, New cementitious materials based on alkali-activated fly ash: performance at high temperatures, J. Am. Ceram. Soc. 91 (10) (2008) 3308–3314, https://doi.org/10.1111/j.1551-2916.2008.02625.x.

[19] A.M. Criado, A. Palomo, A. Fernandez-Jimenezw, Alkali activated fly ash: effect of admixtures on paste rheology, Original Contrib. 48 (1) (2009) 447–455, https://doi.org/10.1007/s00397-008-0345-5.

[20] X.Z. Lu, J.G. Teng, L.P. Ye, J.J. Jiang, Bond–slip models for FRP sheets/plates bonded to concrete, Eng. Struct. 27 (6) (2005) 920–937, https://doi.org/10.1016/j.engstruct.2005.01.014.

[21] J.F. Chen, J.G. Teng, Anchorage strength models for FRP and steel plates bonded to concrete, J. Struct. Eng. 127 (7) (2001) 784–791, https://doi.org/10.1061/(ASCE)0733-9445(2001)127:7(784).

[22] J. Yao, J.G. Teng, J.F. Chen, Experimental study on FRP-to-concrete bonded joints, Compos. B Eng. 36 (2) (2005) 99–113, https://doi.org/10.1016/j.compositesb.2004.06.001.

[23] T. Cardinale, C. Sposato, A. Feo, P. De Fazio, Clay and fibers: energy efficiency in buildings between tradition and innovation, Math. Model. Eng. Probl. 5 (3) (2018) 183–189, https://doi.org/10.18280/mmep.050308.